Time-Dependent Elastic Tensor of Cellulose Nanocrystal Probed by Hydrostatic Pressure and Uniaxial Stretching

Guangjie Song,[†] Christine Lancelon-Pin,[‡] Pan Chen,[¶] Jian Yu,[†] Jun Zhang,[*,†] Lei Su,[*,§] Masahisa Wada,[∥] Tsunehisa Kimura,[∥,⊥] and Yoshiharu Nishiyama[*,‡]

[†]*Beijing National Laboratory for Molecular Sciences, CAS Key Laboratory of Engineering Plastics, Institute of Chemistry, Chinese Academy of Sciences (CAS), Beijing 100190, China*

[‡]*Univ. Grenoble Alpes, CNRS, CERMAV, 38000 Grenoble, France*

[¶]*Beijing Engineering Research Center of Cellulose and its Derivatives, School of Materials Science and Engineering, Beijing Institute of Technology, 5 South Zhongguancun Street, Haidian District, Beijing 100081, China*

[§]*CAS Key Laboratory of Photochemistry, Institute of Chemistry, Chinese Academy of Sciences (CAS), Beijing 100190, China*

[∥]*Division of Forest and Biomaterials Science, Kyoto University, Sakyo-ku, Kyoto 606-8502, Japan*

[⊥]*Fukui University of Technology, 3-6-1 Gakuen, Fukui 910-8505, Japan*

E-mail: jzhang@iccas.ac.cn; leisu2050@iccas.ac.cn; yoshi@cermav.cnrs.fr

Contents

1 Strain tensor calculated from displacements of diffraction peaks

1.1 Calculation of transformation tensor

The transformation tensor $\mathbf{F}$ transforms the pre-deformation vector $\mathbf{v}$ to the post-deformation vector $\mathbf{v}'$:

$$\mathbf{v}' = \mathbf{F}\mathbf{v}. \tag{S1}$$

This gives the Lagrange strain tensor $\mathbf{E}$ as

$$\mathbf{E} = \frac{\mathbf{1}}{\mathbf{2}}\left(\mathbf{F^T F} - \mathbf{I}\right). \tag{S2}$$

In the three-dimensional case, given three sets of independent vectors, $\mathbf{F}$ is

$$(\mathbf{v_0'}, \mathbf{v_1'}, \mathbf{v_2'}) = \mathbf{F}(\mathbf{v_0}, \mathbf{v_1}, \mathbf{v_2}) \tag{S3}$$

and thus

$$\mathbf{F} = (\mathbf{v_0'}, \mathbf{v_1'}, \mathbf{v_2'})(\mathbf{v_0}, \mathbf{v_1}, \mathbf{v_2})^{-\mathbf{1}}. \tag{S4}$$

1.2 Monoclinic system

For the monoclinic case, the symmetry allows the fiber axis to be directly separated from the other directions. The experimental data reveal three intense equatorial reflections and a single meridian reflection, making four sets of scalar values, which are sufficient to determine a unique deformation: The fiber axis direction can be treated independently, so the problem reduces to one of determining a two-dimensional deformation with three lengths. From the reciprocal lattice, we choose three lattice points that are in plane perpendicular to the fiber axis and are not parallel to each other. Here, $\mathbf{p}_0 = (1\bar{1}0)$, $\mathbf{p}_1 = (110)$ and $\mathbf{p}_2 = (200)$. Since

$$\mathbf{p}_2 = \mathbf{p}_0 + \mathbf{p}_1, \tag{S5}$$

we can use the three lengths $|\mathbf{p}_i|$ to determine the relative direction of the three vectors. We define the coordinates of $\mathbf{p}_2$ to be

$$\mathbf{p}_2 = (p_2, 0, 0) \tag{S6}$$

and determine the coordinates of $\mathbf{p}_1$ to be

$$\mathbf{p}_1 = (x, y, 0), \tag{S7}$$

where

$$x = \frac{\mathbf{p}_1 \cdot \mathbf{p}_2}{p_2} = \frac{{p_1}^2 + {p_2}^2 - {p_0}^2}{2p_2}, \tag{S8}$$

and

$$y = \frac{2A}{p_2}, \tag{S9}$$

where A is the area of the triangle p_0, p_1, p_2:

$$A = \frac{\sqrt{(p_0 + p_1 + p_2)(p_0 + p_1 - p_2)(p_0 - p_1 + p_2)(-p_0 + p_1 + p_2)}}{4}. \tag{S10}$$

The xy plane component of the transformation tensor

$$F_{xy} = \begin{pmatrix} p_2' & x' \\ 0 & y' \end{pmatrix} \begin{pmatrix} p_2 & x \\ 0 & y \end{pmatrix}^{-1} \tag{S11}$$

$$= \frac{1}{p_2 y} \begin{pmatrix} p_2' & x' \\ 0 & y' \end{pmatrix} \begin{pmatrix} y & -x \\ 0 & p_2 \end{pmatrix} \tag{S12}$$

$$= \frac{1}{p_2 y} \begin{pmatrix} p_2' y & -p_2' x + p_2 x' \\ 0 & p_2 y' \end{pmatrix} \tag{S13}$$

$$= \begin{pmatrix} \frac{p_2'}{p_2} & -\frac{p_2' x}{p_2 y} + \frac{x'}{y} \\ 0 & \frac{y'}{y} \end{pmatrix}, \tag{S14}$$

and the strain tensor

$$E = \frac{1}{2}\left(F^T F - I\right) \tag{S15}$$

$$= \frac{1}{2}\left(\begin{pmatrix} f_0 & 0 \\ f_1 & f_2 \end{pmatrix}\begin{pmatrix} f_0 & f_1 \\ 0 & f_2 \end{pmatrix} - I\right) \tag{S16}$$

$$= \frac{1}{2}\begin{pmatrix} f_0^2 - 1 & f_0 f_1 \\ f_0 f_1 & f_1^2 + f_2^2 - 1 \end{pmatrix}, \tag{S17}$$

where

$$f_0 = \frac{p_2'}{p_2}, \tag{S18}$$

$$f_1 = -\frac{p_2' x}{p_2 y} + \frac{x'}{y}, \tag{S19}$$

$$f_2 = \frac{y'}{y}. \tag{S20}$$

1.3 Eigenvalues and eigenvectors

Given a strain tensor

$$E = \begin{pmatrix} a & b \\ b & c \end{pmatrix}, \tag{S21}$$

the eigenvalue λ can be obtained by solving the determinant equation

$$|E - \lambda I| = (a-\lambda)(c-\lambda) - b^2 \tag{S22}$$

$$= \lambda^2 - (a+c)\lambda + ac - b^2 = 0, \tag{S23}$$

$$\lambda = \frac{(a+c) \pm \sqrt{(a+c)^2 - 4(ac - b^2)}}{2} \tag{S24}$$

$$= \frac{(a+c) \pm \sqrt{(a-c)^2 + 4b^2}}{2}. \tag{S25}$$

The eigenvectors are

$$\begin{pmatrix} \lambda - a \\ b \end{pmatrix} = \begin{pmatrix} \frac{c-a \pm \sqrt{(a-c)^2+4b^2}}{2} \\ b \end{pmatrix}, \tag{S26}$$

or the angle θ of the eigenvectors with respect to $\mathbf{p}_2$ is

$$\theta = \mathrm{atan}\left(\frac{c - a \pm \sqrt{(a-c)^2 + b^2}}{2b}\right). \tag{S27}$$

1.4 Error estimates

The nonlinear least-squares fit to the diffraction data provides estimates of the error in the peak position. However, compared with the apparent fluctuations of measured values around the tendency, these estimates are in general very small for a single profile. Because we do not have multiple measurements for each data point, we use subsets of two-dimensional diffraction data to estimate the experimental error in the peak position.

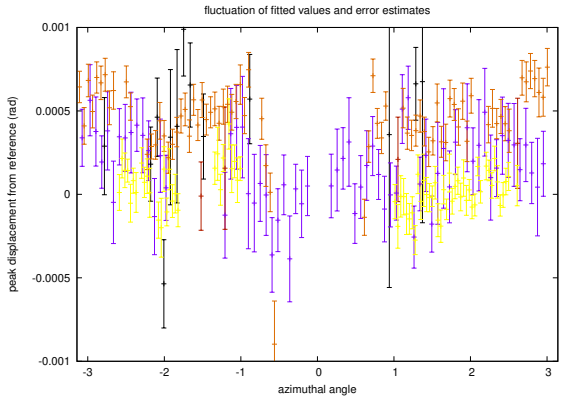

Figure S1: Peak displacement with respect to reference position (°) as a function of azimuthal angle (rad). Colors correspond to different peaks.

Figure 1 presents the result of a fit to the peaks of the diffraction rings from the file "CNF_0002.tiff" as a function of azimuthal angle. In short, all pixels within 10 pixels of the expected radius were selected and sorted according to azimuthal angle. Next, 300 pixels were used for each fit to fit against a Gaussian peak with a linear baseline. The fitted positions are plotted as a function of azimuthal angle, with the error estimates included. In this file, the average counting per pixel was about 40, and the peak height of 1–10 reflections (see black points in Fig. S1) was in the range of 3–10 counts, but the estimated errors remained relatively low. However, the fluctuation in position exceeds by far the estimated error.

In the next step, we use the fluctuations in position to evaluate the weighted average and its standard error. Given that the use of variance to weight individual points assigns too much weight to a small number of points, the values were instead weighted by the reciprocal of the standard error.

The weighted average $\bar{x}$ and standard deviation σ are

$$\bar{x} = \frac{\sum w_i x_i}{\sum w_i}, \tag{S28}$$

$$\sigma = \sqrt{\left(\frac{\sum w_i {x_i}^2}{\sum w_i} - (\bar{x})^2\right) \frac{\sum({w_i}^2)}{\left(\sum w_i\right)^2 - \sum({w_i}^2)}}. \tag{S29}$$

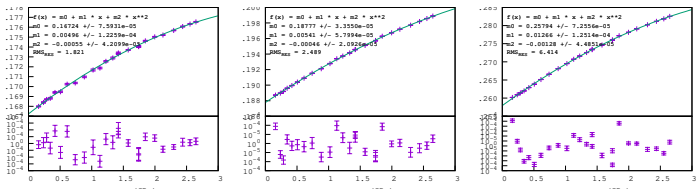

Figure S2: Peak position as a function of pressure and fit to a parabolic function. Residuals of the fit are shown in the bottom panels.

Figure S2 shows the peak position with estimated error as a function of pressure evaluated just discussed. The solid curve is a weighted linear least-squares fit to a parabolic function

$$f(x) = m_0 + m_1 x + m_2 x^2, \tag{S30}$$

with the residuals shown in the bottom panels. The residuals show no systematic tendencies, which suggests that the simple parabolic function is a good approximation of the tendency. However, the root mean square of residuals is greater than unity, which indicates that the measurement error associated with each peak position is likely underestimated. To compensate for this underestimation, the error estimates are multiplied by the root mean square of the fit in the following. Each peak

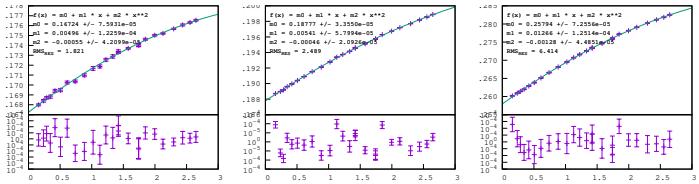

Figure S3: Same as Fig. S2 but with the error scaled by the root mean square of the residuals.

position is associated with an independent estimated error δp_i. For the reciprocal coordinates, in Eq. [7], the error estimation is simple:

$$\frac{\delta_x}{|x|} = \sqrt{\frac{{\delta_{({p_1}^2+{p_2}^2-{p_0}^2)}}^2}{({p_1}^2+{p_2}^2-{p_0}^2)^2} + \frac{{\delta_2}^2}{{p_2}^2}}, \tag{S31}$$

where

$$\delta_{({p_1}^2+{p_2}^2-{p_0}^2)}{}^2 = \sum \delta({p_i}^2)^2 = \sum 4{p_i}^2{\delta_i}^2, \tag{S32}$$

$$\frac{\delta_y}{|y|} = \sqrt{\frac{\sum {\delta_i}^2}{2}\left(\sum \frac{1}{{s_i}^2}\right) + \left(\frac{\delta_2}{p_2}\right)^2}. \tag{S33}$$

However, the analytical solution for the tensors is complex, so we numerically estimate the propagation error. Any member f of the deformation and strain tensor depends on the three lengths p_i before deformation and on p_i' after deformation, which makes a total of six experimental measurements. The error estimate is

$$\delta f = \sqrt{\sum^{6}\left(\frac{\partial f}{\partial p_i}\delta p_i\right)^2}, \tag{S34}$$

where numerically,

$$\left(\frac{\partial f}{\partial p_i}\delta p_i\right)^2 = \left[f(p_i+\delta_i) - f(p_i)\right]^2. \tag{S35}$$

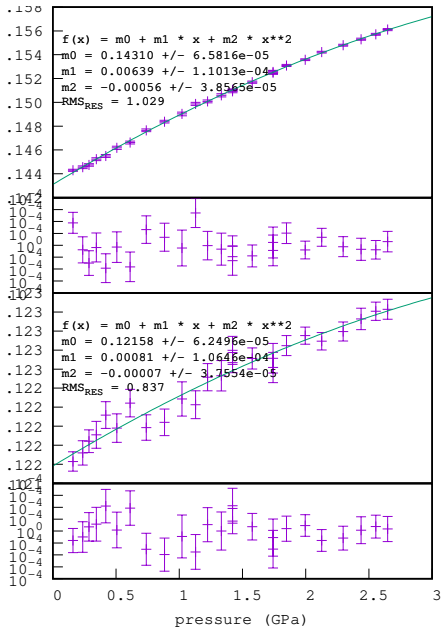

Figure S4: Position of vector 110 according to Eqs. [8] and [9].

The elastic tensor relates strain and stress as follows:

$$\epsilon = S\sigma, \tag{S36}$$

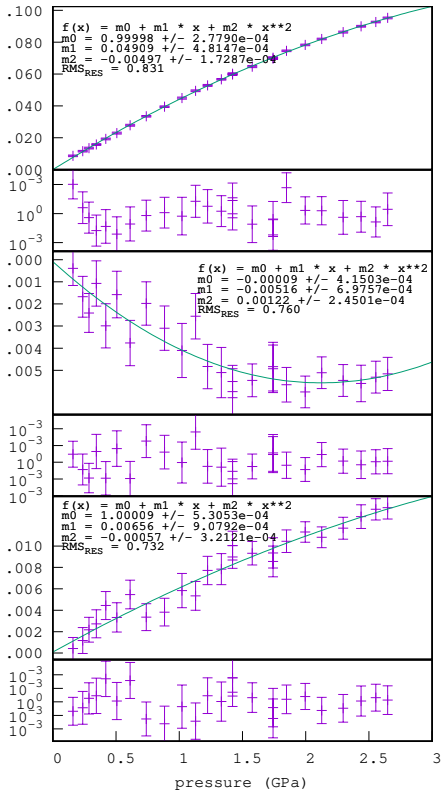

Figure S5: Deformation tensor of Eq. [14].

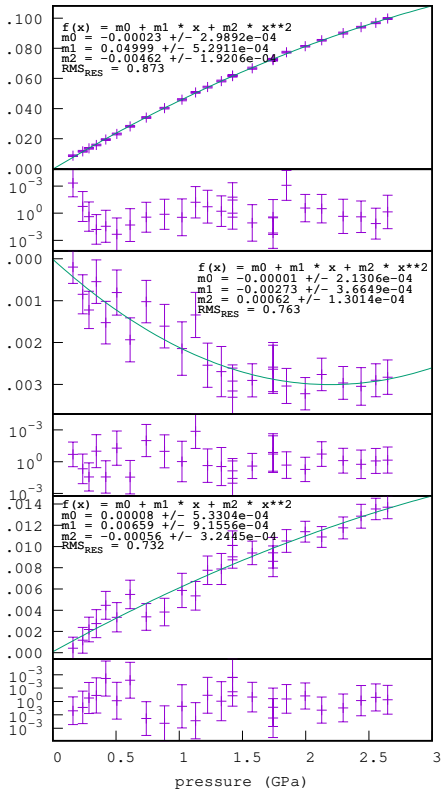

Figure S6: Lagrange strain tensor of Eqs. [18]–[20].

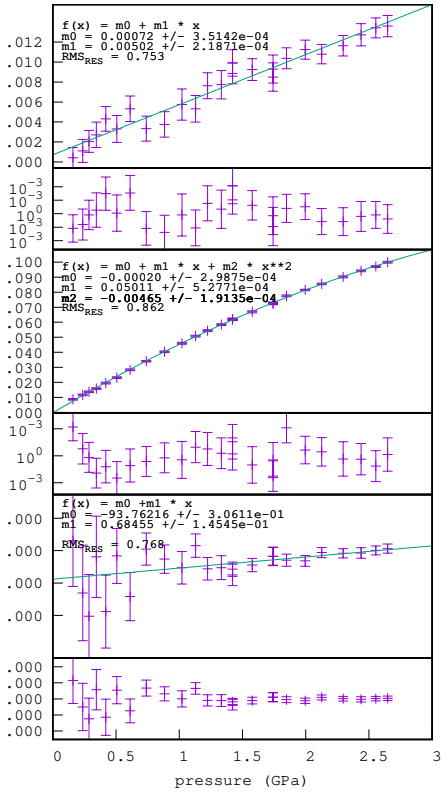

Figure S7: Eigenvalues of Lagrange strain and the eigenvector direction according to Eqs. [25] and [27].

where S is the compliance matrix. For P21 systems, in continuum mechanics,

$$S = \begin{pmatrix} s_{11} & s_{12} & s_{13} & 0 & 0 & s_{16} \\ s_{21} & s_{22} & s_{23} & 0 & 0 & s_{26} \\ s_{31} & s_{32} & s_{33} & 0 & 0 & s_{36} \\ 0 & 0 & 0 & s_{44} & s_{45} & 0 \\ 0 & 0 & 0 & s_{54} & s_{55} & 0 \\ s_{61} & s_{62} & s_{63} & 0 & 0 & s_{66} \end{pmatrix}. \tag{S37}$$

From the hydrostatic experiment, we experimentally obtain the relation

$$\begin{pmatrix} \epsilon_1 \\ \epsilon_2 \\ \epsilon_3 \\ \epsilon_6 \end{pmatrix} = \begin{pmatrix} s_{11} & s_{12} & s_{13} \\ s_{22} & s_{22} & s_{23} \\ s_{31} & s_{32} & s_{33} \\ s_{61} & s_{62} & s_{63} \end{pmatrix} \begin{pmatrix} \sigma \\ \sigma \\ \sigma \end{pmatrix}, \tag{S38}$$

and from the uniaxial stretching experiment of composite fiber, assuming that all macroscopic stress

is transmitted as uniaxial stretching to the crystals, we obtain

$$\begin{pmatrix} \epsilon'_1 \\ \epsilon'_2 \\ \epsilon'_3 \\ \epsilon'_6 \end{pmatrix} = a\sigma' \begin{pmatrix} s_{13} \\ s_{23} \\ s_{33} \\ s_{36} \end{pmatrix}, \tag{S39}$$

where a is the fraction of tensile stress loaded on the crystals.

1.5 Monitoring the beam drift based on tilted fiber patterns

For the equatorial reflections, because the detector covers the opposite side, the drift in the vertical direction (perpendicular to the fiber) can be directly followed by averaging the opposing peaks. Consider, for example, the 2 0 0 peak position in pixels during a cyclic stretching with variable amplitude and of a total duration of 2 hours. The difference between the two positions gives the drift of the central position, which can be up to 0.2 pixels in this direction, whereas the amplitude of the peak shift goes up to 1.6 pixels. The drift in the direct beam can be further canceled by averaging the positions of opposing peaks. The drift in fiber direction is more delicate because the

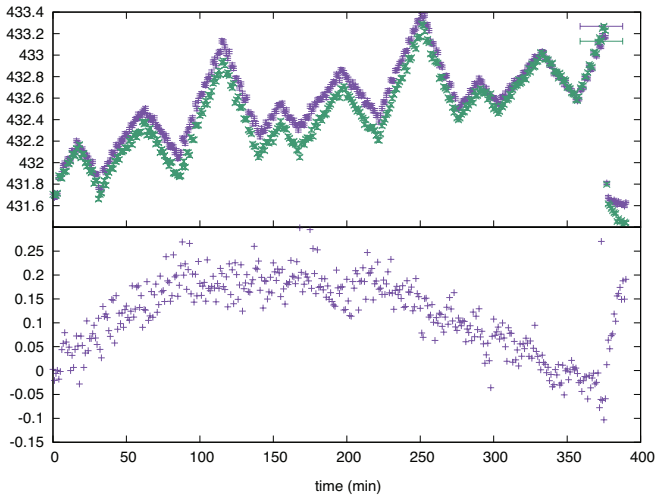

Figure S8: Radial peak positions of two opposing equatorial 2 0 0 reflections and their difference.

meridian reflection appears only on one side, given that the fiber is tilted to bring the peak into the Bragg condition. We thus use layer line reflections to follow the beam drift, namely, the 0 1 2/1 0 2 composite peak. Four equivalent reflections can be followed on the detector and are arranged with axial symmetry but without point symmetry around the center. To obtain the drift, we consider how

the center drift and lattice variations affect the peak positions. For reflection i at azimuthal angle β_i, if the beam center drifts by (dx, dy), the observed change dr_i in radial position with respect to the reference position is

$$dr'_i = dx \sin(\beta_i) + dy \cos(\beta_i) + dr, \tag{S40}$$

where dr is the change due to a change in d spacing. In matrix form, we have

$$\begin{pmatrix} dr'_1 \\ dr'_2 \\ dr'_3 \\ dr'_4 \end{pmatrix} = \begin{pmatrix} \sin\beta_1 & \cos\beta_1 & 1 \\ \sin\beta_2 & \cos\beta_2 & 1 \\ \sin\beta_3 & \cos\beta_3 & 1 \\ \sin\beta_4 & \cos\beta_4 & 1 \end{pmatrix} \begin{pmatrix} dx \\ dy \\ dr \end{pmatrix}, \tag{S41}$$

so dx, dy, dr may be obtained by solving a linear least-squares problem of the form

$$b = Ax. \tag{S42}$$

This is done by using the DGELSY driver of the linear algebra package LAPACK.[1]

In this case, the beam drifts by about 0.2 pixels in the equatorial direction and by about 0.1 pixels in the meridian direction. The drift in the equatorial direction can be canceled by taking the average of opposing reflections. For the 0 0 4 position, the peak shifts by 4.5 pixels, so the contribution of drift can account for at most a 2% error in the estimate of the modulus in the c direction.

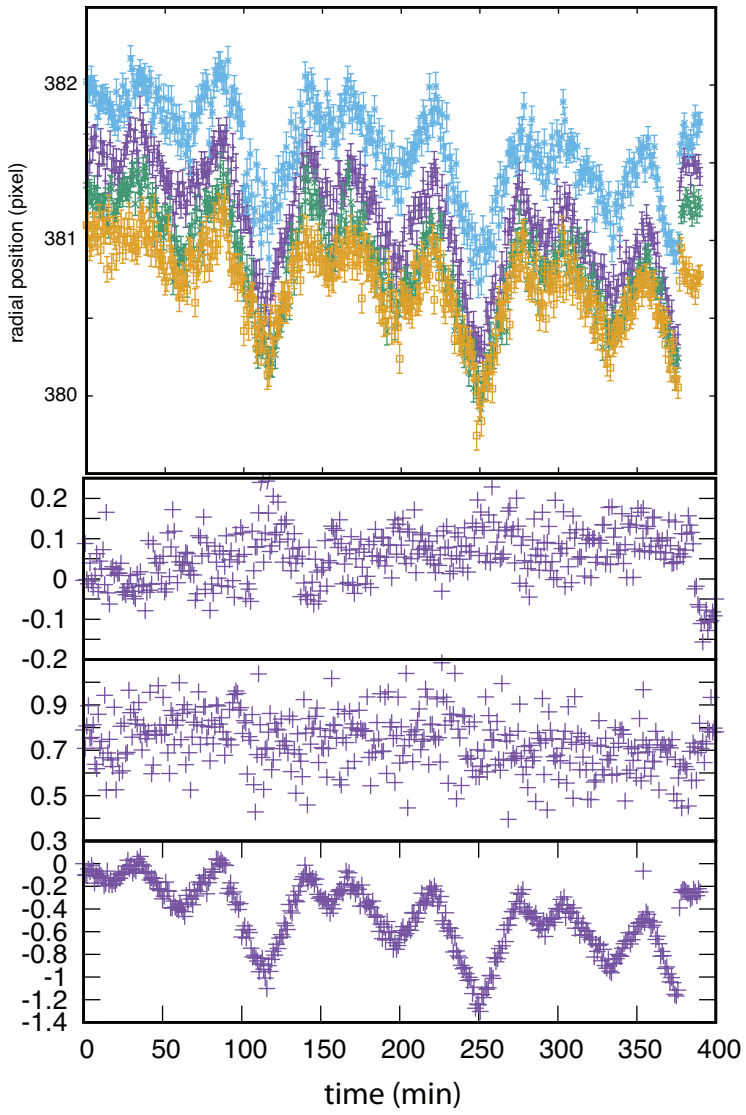

Figure S9: Peak positions of four equivalent reflections, the corresponding center drift in the x and y directions, and the shift due to the change in diffraction angle, all as functions of frame number.

2 X-ray diffraction experiments on samples under hydrostatic pressure

Three x-ray diffraction measurements were made, each under slightly different conditions. Table S1 lists the resulting compressibilities and the associated conditions. Data sets data 1 and data 2 have similar values, although data 1 is much more accurate. Data 3 indicates significantly lower compressibility for $X1$ and $X3$. However, the data not only were measured under high loading but also suffered from broader peak widths, which might be due to internal stress that could come from drying or from the sample touching the cell, which would create frictional forces.

Table S1: The experimental compressibility of the I_β crystal and the setup parameters of experiments

	Unit	Data 1	Data 2	Data 3
$X1$		49.6 ± 0.4	51.8 ± 2.2	38 ± 0.6
$X2$		6.5 ± 1	6.4 ± 1.0	8.3 ± 0.9
$X3$	TPa^{-1}	1.71 ± 0.02	2.3 ± 1.8[a]	1.3 ± 0.2 [a]
			1.6 ± 0.05 [b]	
$X6$		-2.6 ± 0.4	-4.1 ± 0.6	5.6 ± 0.5
$X1'$		4.5 ± 0.2	6.3 ± 0.7	2.3 ± 0.2
$X2'$	x1000	0.5 ± 0.3	0.45 ± 0.35	2 ± 0.3
$X3'$	TPa^{-1}	0	0	0
			0	1 ± 0.1
$X6'$		0.6 ± 0.1	-1.1 ± 0.2	-1.1 ± 0.2
Beamline		Beijing BL4W2	Shanghai BL1SU	Beijing BL4W2
Detector		Pilatus3 2M	MAR165 CCD	Pilatus3 2M
Pixel size	μm	172	80	172
Beamsize (H × V)	μm	36×14	5×5	36×14
Sample-to-detector distance	mm	285	202	285
Wavelength	Å	0.6199	0.6199	0.6199
Peak width $(1\,\bar{1}\,0)$	deg	0.260 ± 0.008	0.217 ± 0.007	0.368 ± 0.003
Peak width $(1\,1\,0)$	deg	0.239 ± 0.002	0.221 ± 0.002	0.295 ± 0.002
Peak width $(2\,0\,0)$	deg	0.264 ± 0.001	0.240 ± 0.002	0.309 ± 0.003
Peak area ratio $(1\bar{1}0/110)$		0.46	0.39	1.54
Pressure range	GPa	0–3	0–10	0–3
Compression rate	MPa/min	6.7	14.35	27.6
Anvil size	μm	800	800	350
Hole size	μm	400	320	150
Pre-indented thickness	μm	130	105	100

[a] Using pressure range 0–3 GPa. [b] Using pressure range 0–8 GPa.

3 Reference frame conversion of elastic tensor

Conversion to $a*bc$ frame

The compliance matrices in Ref.[2] are defined in the $ab*c$ frame because it is the most common crystallographic axis convention. In the experiment on cellulose I$_b$*eta*, we used the reference frame $a*bc$, which is rotated by 6.5°around the z axis with respect to $ab*c$, and thus tensor rotation operation

$$s' = K_z^T s K_z \tag{S43}$$

must be applied to compare our results with the tensors reported in the literature. Here, s' and s is the tensor matrix in the new and original reference frame, respectively, and K is the rotation matrix, which is defined as

$$K = \begin{pmatrix} \cos\theta^2 & \sin\theta^2 & 0 & 0 & 0 & 2\sin\theta\cos\theta \\ \sin\theta^2 & \cos\theta^2 & 0 & 0 & 0 & -2\sin\theta\cos\theta \\ 0 & 0 & 1 & 0 & 0 & 0 \\ 0 & 0 & 0 & \cos\theta & \sin\theta & 0 \\ 0 & 0 & 0 & -\sin\theta & \cos\theta & 0 \\ -\cos\theta\sin\theta & \cos\theta\sin\theta & 0 & 0 & 0 & \cos\theta^2 - \sin\theta^2 \end{pmatrix}, \tag{S44}$$

where $\theta = 6.5°$ is the rotation angle. Applying this rotation to Ref.[2] results in the tensor matrix

$$s_{dri2013}[TP^{-1}](at300K) = \begin{pmatrix} 65.8 & -3.3 & -1.1 & 0 & 0 & 17.6 \\ -3.3 & 11.8 & -0.15 & 0 & 0 & -8.1 \\ -1.1 & -0.15 & 5.1 & 0 & 0 & -1 \\ 0 & 0 & 0 & 95.4 & -125.7 & 0 \\ 0 & 0 & 0 & -125.7 & 510.8 & 0 \\ 17.6 & -8.1 & -1 & 0 & 0 & 343.8 \end{pmatrix}. \tag{S45}$$

Reference[3] also apparently uses the $a*bc$ frame but does not seem to follow the conventional Voigt convention ordering the shear as $s23$, $s31$, $s12$, but instead uses $s12$, $s23$, $s31$. Upon changing

the order and applying the rotation, we obtain

$$s_{\text{Eichhorn2006}} = \begin{pmatrix} 52.9 & -9.3 & -1.8 & 0 & 0 & -17.5 \\ -9.5 & 21.3 & -1.3 & 0 & 0 & 31.1 \\ -1.18 & -1.3 & 6.8 & 0 & 0 & -1.8 \\ 0 & 0 & 0 & -4.6 & 40.6 & 0 \\ 0 & 0 & 0 & 40.6 & -16.5 & 0 \\ -16.8 & 29.5 & -2 & 0 & 0 & 306.4 \end{pmatrix}.$$

The negative diagonal elements indicate that this tensor has a problem in the shear components, which is the consequence of larger off-diagonal elements in the stiffness matrix. The method of deducing this tensor was not reported in Ref.[3]

4 Poisson's ratio during fast deformation

Poisson's ratios were also calculated from each loading and unloading process during the cyclic tensile experiment (see Fig. S10) using a linear least-squares regression. The result is summarized in Table S2.

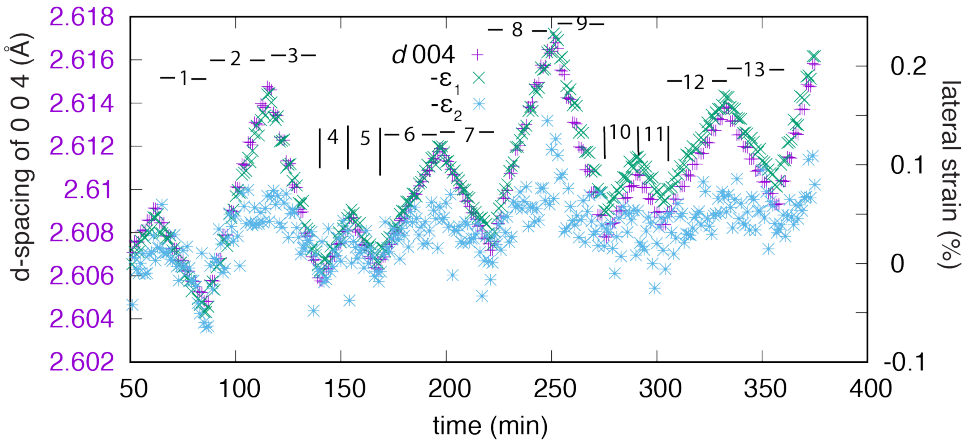

Figure S10: Segments used to measure Poisson's ratio under cyclic loading.

Table S2: Poisson's ratios from fast deformations.

Segment	ν_{31}	ν_{31}
1	0.561 ± 0.006	0.248 ± 0.032
2	0.514 ± 0.005	0.203 ± 0.030
3	0.529 ± 0.020	0.088 ± 0.137
4	0.540 ± 0.022	0.072 ± 0.147
5	0.537 ± 0.007	0.207 ± 0.040
6	0.512 ± 0.012	0.252 ± 0.064
7	0.542 ± 0.006	0.225 ± 0.031
8	0.517 ± 0.004	0.163 ± 0.037
9	0.503 ± 0.014	0.159 ± 0.120
10	0.488 ± 0.015	0.140 ± 0.185
11	0.508 ± 0.007	0.175 ± 0.043
12	0.516 ± 0.007	0.091 ± 0.061
13	0.518 ± 0.006	0.221 ± 0.036
Weighted average	0.524 ± 0.005	0.20 ± 0.01

[a] Corresponds to Fig. S10.

5 Theoretical estimate of elastic tensor by modeling

5.1 Density functional theory calculation with strain combinations to determine tensor

Both the experimental unit cell and the atomic coordinates of cellulose I_β [4] were firstly optimized using periodic density functional theory (DFT) calculations at 1 bar of pressure applied in the xyz dimensions. The kinetic energy cutoff was 70 Ry, and the k-grid dimension was $2 \times 2 \times 2$. The convergence criteria for total energy and force were set to 10^{-6} Ry and 10^{-5} Ry/bohr, respectively. Based on the monoclinic unit cell and $P2_1$ symmetry, 13 combinations of initial strain deformations (see Table S3) were generated by the elastic package[5] to deduce the 13 corresponding tensor elements (see Table S4). The strain unit η at each deformation varied linearly from -0.01 to 0.01 in increments of 0.001 and contained 21 frames in all. DFT-based energy minimization of only atomic coordinates for each deformed structure (not the unit cell) was done by using the QUANTUM ESPRESSO package (QE),[6,7] version 6.6, which uses the generalized gradient approximation, the Perdew-Burke-Ernzerhof functional,[8] and the pairwise DFT-D2 correction for long-range van der Walls dispersion.[9] We used the energy-strain approach[5] to estimate the elastic tensor of crystalline cellulose I_β.

Table S3: The symmetric strain components of 13 deformation modes.

Deformation mode	xx	yy	zz	yz	xz	xy
1	η	η	η	0	0	0
2	0.5η	$-\eta$	0.5η	0	0	0
3	$-\eta$	0.5η	0.5η	0	0	0
4	η	$-\eta$	0	0	0	2η
5	0	η	$-\eta$	0	0	2η
6	η	$-\eta$	0	0	0	0
7	0	0	0	2η	2η	0
8	η	0	0	0	0	η
9	0	η	0	0	0	0
10	0	0	η	0	0	0
11	0	0	0	2η	0	0
12	0	0	0	0	2η	0
13	0	0	0	0	0	2η

Table S4: Derivative $\mathrm{d}\sigma/\mathrm{d}\eta$ of the output stress tensor.

	xx	sd_{xx}	yy	sd_{yy}	zz	sd_{zz}	yz	sd_{yz}	xz	sd_{xz}	xy	sd_{xy}
1	40.80	0.64	126.00	−1.79	233.00	2.25	0.00	0.00	0.00	0.00	−7.73	0.0405
2	1.59	0.20	−87.90	−0.60	97.20	0.39	0.00	0.01	0.00	0.00	9.75	0.089
3	−6.08	0.46	43.90	−0.19	99.40	0.44	0.00	0.00	0.00	0.00	−3.35	0.0979
4	5.81	0.19	−105.00	−0.89	0.73	0.44	0.01	0.00	0.01	0.00	19.00	0.109
5	1.89	0.11	68.10	−0.38	−191.00	0.53	−0.01	0.01	0.00	0.00	−0.80	0.156
6	5.56	0.29	−88.00	−0.49	−1.89	0.37	0.00	0.00	0.00	0.00	8.94	0.0929
7	0.01	0.11	0.02	−0.19	−0.01	0.15	−30.70	0.07	2.62	0.05	0.00	0.0768
8	18.00	0.20	−4.84	−0.22	14.30	0.49	0.00	0.01	0.00	0.00	9.50	0.106
9	12.60	0.13	101.00	−0.82	13.30	0.21	−0.01	0.00	0.00	0.00	−9.22	0.0917
10	10.20	0.33	13.20	−0.26	206.00	0.77	0.01	0.01	0.00	0.01	1.41	0.0644
11	0.04	0.04	0.07	−0.12	0.00	0.20	−31.70	0.12	−1.38	0.03	0.00	0.0259
12	0.00	0.07	−0.04	−0.05	0.05	0.05	1.38	0.05	4.29	0.02	0.01	0.0194
13	0.44	0.11	−18.10	−0.15	2.10	0.13	0.01	0.01	0.00	0.00	9.76	0.0509

[a] Stress elements given in units of GPa.

The calculated stiffness tensor is

$$C_{ij}[\mathrm{GPa}] = \begin{pmatrix} 24.2 & 14.7 & 11.6 & 0 & 0 & -1.5 \\ 14.7 & 100.6 & 8.1 & 0 & 0 & -10.6 \\ 11.6 & 8.1 & 207.5 & 0 & 0 & 2.6 \\ 0 & 0 & 0 & 16.2 & -0.5 & 0 \\ 0 & 0 & 0 & -0.5 & 2.3 & 0 \\ -1.5 & -10.6 & 2.6 & 0 & 0 & 5.0 \end{pmatrix}. \tag{S46}$$

The compliance matrix is

$$S_{ij}[\mathrm{TPa}^{-1}] = \begin{pmatrix} 46.39 & -6.43 & -2.37 & 0 & 0 & 1.36 \\ -6.43 & 13.80 & -0.52 & 0 & 0 & 27.46 \\ -2.37 & -0.52 & 5.03 & 0 & 0 & -4.38 \\ 0 & 0 & 0 & 62.03 & 14.23 & 0 \\ 0 & 0 & 0 & 14.23 & 431.52 & 0 \\ 1.35 & 27.46 & -4.38 & 0 & 0 & 259.88 \end{pmatrix}. \tag{S47}$$

The asymmetric compliance matrix is

$$S_{ij}[\mathrm{TPa}^{-1}] = \begin{pmatrix} 64.51 & -9.44 & -2.65 & -0.05 & 0.11 & -19.14 \\ -8.99 & 13.41 & -0.59 & -0.02 & 0.05 & 25.24 \\ -2.90 & -0.46 & 5.00 & 0.01 & -0.05 & -1.82 \\ -0.02 & 0.00 & 0.00 & 63.61 & 19.96 & 0.04 \\ -0.04 & 0.01 & 0.00 & 21.90 & 476.52 & -0.03 \\ -12.02 & 24.65 & -2.78 & -0.06 & -0.48 & 250.58 \end{pmatrix}. \tag{S48}$$

The SD matrix of the asymmetric compliance matrix is

$$\text{SD of } S_{ij}[\mathrm{TPa}^{-1}] = \begin{pmatrix} 0.55 & 0.15 & 0.04 & 0.06 & 1.14 & 0.99 \\ 0.22 & 0.07 & 0.02 & 0.09 & 0.22 & 0.43 \\ 0.04 & 0.01 & 0.01 & 0.01 & 0.02 & 0.04 \\ 0.03 & 0.01 & 0.00 & 0.28 & 1.48 & 0.06 \\ 0.12 & 0.04 & 0.01 & 0.84 & 4.55 & 0.28 \\ 1.79 & 0.48 & 0.14 & 0.45 & 2.14 & 3.04 \end{pmatrix}. \tag{S49}$$

5.2 Density functional theory calculation of cellulose under hydrostatic pressure

Based on the unit cell and atomic coordinates optimized for cellulose I_β, the crystal was further relaxed under a series of pressure, which was increased up to 3 GPa in a step-wise manner with a step size of 0.3 GPa. At the convergence of each step, the optimized unit cell parameters were extracted. The compressibility was estimated based on the linear slope between the optimized unit cell parameters and the applied pressure.

5.3 Density functional theory simulation of uniaxial loading

Starting from the relaxed unit cell and atomic coordinates, the unit-cell parameter c (parallel to the z direction) was compressed and elongated by up to 1% from 0.1% during the DFT calculation, for a total 21 frames. By using "2Dxy" implemented in QE, the c length was fixed, but the parameters a, b and γ were allowed to relax. Such a strategy allows us to simulate the uniaxial loading of

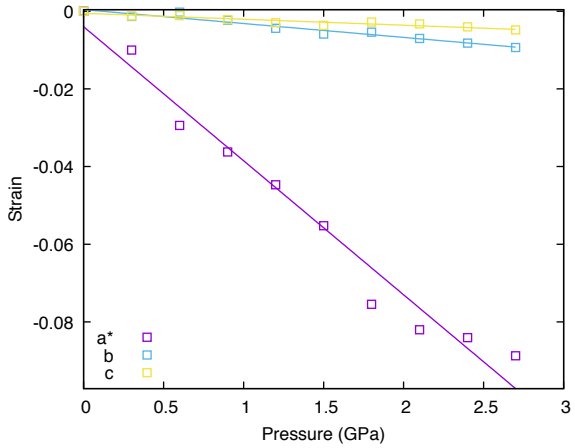

Figure S11: Relative deformation of unit cell length under pressure obtained by DFT minimization.

crystals in the c-axis (fiber) direction. To simulate uniaxial loading in the $a*$ direction, we rotate the coordinates to place $\mathbf{a}*$ parallel to z axis, **b** parallel to x,and **c** parallel to y axis. The QE code was hacked by inserting two lines into to the 2Dxy section [$iforceh(1,3) = 1$ and $iforceh(2,3) = 1$, which fixed the z coordinate of the a axis but leaving both its x and y coordinates free to refine.

Molecular dynamics simulation of cellulose $\mathbf{I}_\beta$

The structure was placed in the simulation box from the experimental unit cell based on x-ray and neutron diffraction data[4] so that the b axis of the unit cell is parallel to the X direction, the c axis is parallel to Z, and the a axis lays in the XY plane. This rotated structure was further extended to make an $8 \times 8 \times 10$ supercell containing a total of 128 chains. Periodic boundary conditions were applied in the xyz direction. Cellulose chains of degree of polymerization of 20 were chemically linked to their mirrors to represent infinite cellulose chains. The crystal was first relaxed by energy minimization by using the steepest descent and conjugated gradient methods, followed by equilibration for 1 ns with a time step of 1 fs. The molecular dynamics simulation was done by using the GROMACS package,[10–12] version 2019, using the GROMOS $56A_{carbo}$ force field[13] together with revised LJ parameters.[14] The temperature was regulated at 300 K by using velocity rescaling[15] and pressure by the Berendsen algorithm.[16] Uniaxial pressure was applied either along the $a*$ direction (which is perpendicular to the bc or yz plane), or along the c direction. The pressure was increased from -10^5 to 10^5 bar in a step-wise manner and with a step size of 10^4 bar. The cutoff for short-range non-bonded interactions was 1.4 nm. The long-range electrostatic interaction was calculated by using the particle mesh Evald (PME) method.[17] Long-range dispersion energy and

pressure were empirically corrected. The compressibility was 2.5×10^5, 2.2×10^5, 7.9×10^7, 1.2×10^5, 4.2×10^5, and 4.2×10^5 bar^{-1} for xx, yy, zz, xy, yz, and zx components, respectively.[18] The OH bond distances were constrained to allow the use of 2 fs time steps for molecular dynamics integration. The production run at each pressure lasted for 10 ns, for which the last 5 ns was used to calculate the optimized unit-cell parameters. The trajectory files were saved every 5 fs. The Poisson's ratios ν_{13} and ν_{31} were estimated based on the slope between the extracted supercell parameters and the applied pressure.

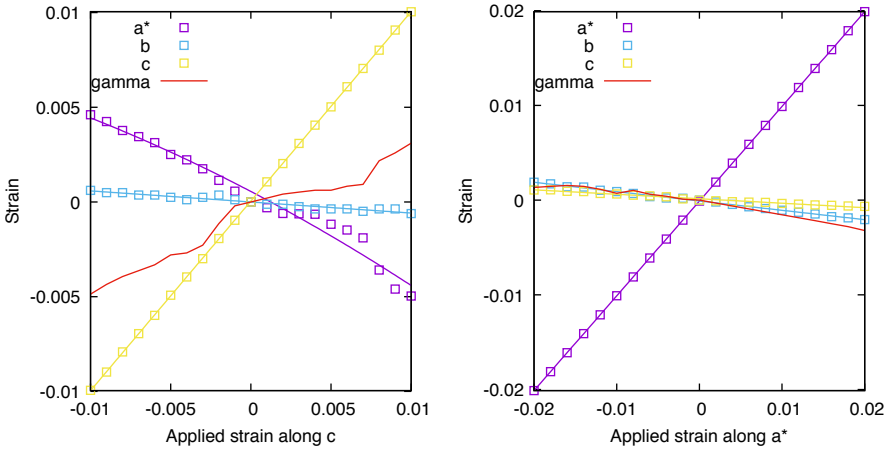

Figure S12: Uniaxial deformation of cellulose I$_\beta$ optimized by using DFT.

Table S5: Parameters obtained by regression in Fig. S12(a).

Loading in c-axis direction	Value	SD
ν_{31}	0.444	0.018
ν_{32}	0.059	0.003
$E33$ [GPa]	202	0.8
$s13$ [TPa^{-1}]	2.2	0.1
$s23$ [TPa^{-1}]	0.3	0.01

Table S6: Parameters obtained by regression in Fig. S12(b).

Loading in $a*$ direction	Value	SD
ν_{12}	0.099	0.001
ν_{13}	0.047	0.001
$E11$ [GPa]	16.3	0.2
$s31$ [TPa^{-1}]	2.9	0.1
$s21$ [TPa^{-1}]	6.1	0.1

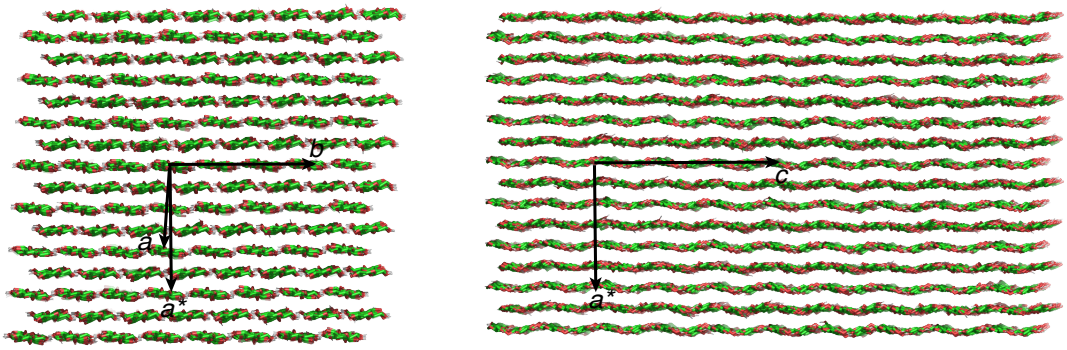

Figure S13: Snapshots of atomic models of cellulose I_β in molecular dynamics simulation.

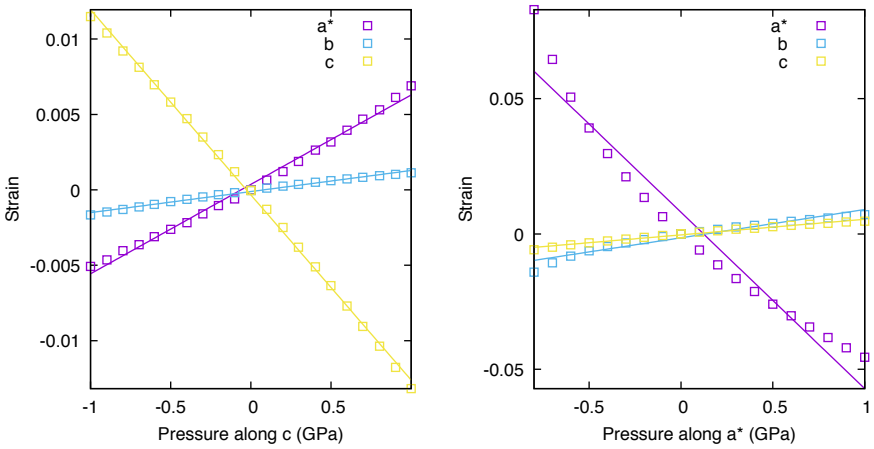

Figure S14: Uniaxial deformation of cellulose I_β optimized by using GROMOS force-field-based molecular dynamics simulation.

Table S7: Parameters estimated by regression in Fig. S14(a).

Loading in c-axis direction	Value	SD
ν_{31}	0.484	0.005
ν_{32}	0.113	0.003
$E33$ [GPa]	81.3	0.6
$s13$ [TPa^{-1}]	5.9	0.1
$s23$ [TPa^{-1}]	1.4	0.03

Table S8: Parameters estimated by regression in Fig. S14(b).

Loading in $a*$ direction	Value	SD
ν_{12}	0.161	0.001
ν_{13}	0.086	0.002
$E11$ [GPa]	14.5	0.2
$s31$ [TPa^{-1}]	5.8	0.2
$s21$ [TPa^{-1}]	10.4	0.7

References

(1) Anderson, E.; Bai, Z.; Bischof, C.; Blackford, S.; Dongarra, J. D. J.; Croz, J. D.; Greenbaum, A.; Hammarling, S.; McKenney, A.; Sorensen, D. *LAPACK Users' Guide*, 3rd ed.; SIAM: Philadelphia, Pennsylvania, USA, 1999.

(2) Dri, F. L.; Jr., L. G. H.; Moon, R. J.; Zavattieri, P. D. Anisotropy of the Elastic Properties of Crystalline Cellulose Iβ from First Principles Density Functional Theory with Van der Waals Interactions. *Cellulose* **2013**, *20*, 2703–2718.

(3) Eichhorn, S. J.; Davies, G. R. Modelling the Crystalline Deformation of Native and Regenerated Cellulose. *Cellulose* **2006**, *13*, 291–307.

(4) Nishiyama, Y.; Langan, P.; Chanzy, H. Crystal Structure and Hydrogen-Bonding System in Cellulose Iβ from Synchrotron X-ray and Neutron Fiber Diffraction. *J. Am. Chem. Soc.* **2002**, *124*, 9074–9082.

(5) Golesorkhtabar, R.; Pavone, P.; Spitaler, J.; Puschnig, P.; Draxl, C. ElaStic: A Tool for Calculating Second-Order Elastic Constants from First Principles. *Computer Physics Communications* **2013**, *184*, 1861–1873.

(6) Giannozzi, P.; Andreussi, O.; Brumme, T.; Bunau, O.; Nardelli, M. B.; Calandra, M.; Car, R.; Cavazzoni, C.; Ceresoli, D.; Cococcioni, M. et al. Advanced Capabilities for Materials Modelling with Quantum ESPRESSO. *J. Phys.: Condens. Matter* **2017**, *29*, 465901.

(7) Giannozzi, P.; Baroni, S.; Bonini, N.; Calandra, M.; Car, R.; Cavazzoni, C.; Ceresoli, D.; Chiarotti, G. L.; Cococcioni, M.; Dabo, I. et al. QUANTUM ESPRESSO: a Modular and Open-Source Software Project for Quantum Simulations of Materials. *Journal of Physics: Condensed Matter* **2009**, *21*, 395502.

(8) Perdew, J. P.; Ernzerhof, M.; Burke, K. Rationale for Mixing Exact Exchange with Density Functional Approximations. *J. Chem. Phys.* **1996**, *105*, 9982–9985.

(9) Grimme, S. Semiempirical GGA-type Density Functional Constructed with a Long-Range Dispersion Correction. *J. Comput. Chem.* **2006**, *27*, 1787–1799.

(10) Hess, B.; Kutzner, C.; van der Speol, D.; Lindahl, E. GROMACS 4:Algorithms for Highly Efficient, Load-balanced, and Scalable Molecular Simulation. *J. Chem. Theory Comput.* **2008**, *4*, 435–447.

(11) Pronk, S.; Páll, S.; Schulz, R.; Larsson, P.; Bjelkmar, P.; Apostolov, R.; Shirts, M. R.; Smith, J. C.; Kasson, P. M.; van der Spoel, D. et al. GROMACS 4.5: a High-Throughput and Highly Parallel Open Source Molecular Simulation Toolkit. *Bioinform.* **2013**, *29*, 845–854.

(12) Abraham, M. J.; Murtola, T.; Schulz, R.; Páll, S.; Smith, J. C.; Hess, B.; Lindahl, E. GROMACS: High Performance Molecular Simulations through multi-level parallelism from laptops to supercomputers. *SoftwareX* **2015**, *1-2*.

(13) Hansen, H. S.; Hünenberger, P. H. A Reoptimized GROMOS Force Field for Hexopyranose-based Carbohydrates Accounting for the Relative Free Energies of Ring Conformers, Anomers, Epimers, Hydroxymethyl Rotamers, and Glycosidic Linkage Conformers. *J. Comput. Chem.* **2011**, *32*, 998–1032.

(14) Chen, P.; Nishiyama, Y.; Mazeau, K. Atomic Partial Charges and one Lennard-Jones Parameter Crucial to Model Cellulose Allomorphs. *Cellulose* **2014**, *21*, 2207–2217.

(15) Bussi, G.; Donadio, D.; Parrinello, M. Canonical Sampling through Velocity Rescaling. *J. Chem. Phys.* **2007**, *126*, 014101.

(16) Berendsen, H. J. C.; Postma, J. P. M.; van Gunsteren, W. F.; DiNola, A.; Haak, J. R. Molecular Dynamics with Coupling to an External Bath. *The Journal of Chemical Physics* **1984**, *81*, 3684–3690.

(17) Darden, T.; York, D.; Pedersen, L. Particle Mesh Ewald: An N·log(N) method for Ewald Sums in Large Systems. *The Journal of chemical physics* **1993**, *98*, 10089–10092.

(18) Chen, P.; Nishiyama, Y.; Mazeau, K. Torsional Entropy at the Origin of the Reversible Temperature-Induced Phase Transition of Cellulose. *Macromolecules* **2012**, *45*, 362–368.